A 122 fps, 1 MHz Bandwidth Multi-Frequency Wearable EIT Belt Featuring Novel Active Electrode Architecture for Neonatal Thorax Vital Sign Monitoring

Yu Wu, *Student Member, IEEE*, Dai Jiang, *Member, IEEE,* Andy Bardill, Richard Bayford, *Member, IEEE*, and Andreas Demosthenous, *Fellow, IEEE*

Abstract—**A highly integrated, wearable electrical impedance tomography (EIT) belt for neonatal thorax vital multiple sign monitoring is presented. The belt has sixteen active electrodes. Each has an application specific integrated circuit (ASIC) connected to an electrode. The ASIC contains a fully differential current driver, a high-performance instrumentation amplifier (IA), a digital controller and multiplexors. The belt features a new active electrode architecture that allows programmable flexible electrode current drive and voltage sense patterns under simple digital control. It provides intimate connections to the electrodes for the current drive and to the IA for direct differential voltage measurement providing superior common-mode rejection ratio. The ASIC was designed in a CMOS 0.35-μm high-voltage technology. The high specification EIT belt has an image frame rate of 122 fps, a wide operating bandwidth of 1 MHz and multi-frequency operation. It measures impedance with 98% accuracy and has less than 0.5 Ω and 1º variation across all possible channels. The image results confirmed the advantage of the new active electrode architecture and the benefit of wideband, multi-frequency EIT operation. The system successfully captured high quality lung respiration EIT images, breathing cycle and heart rate. It can also provide boundary shape information using an array of MEMS sensors interfaced to the ASICs.**

Index Terms—**Active electrode, electrical impedance tomography (EIT), heart rate, integrated circuits, lung respiration monitoring, boundary shape sensing, wearable EIT belt.**

I. INTRODUCTION

ELECTRICAL impedance tomography (EIT) is an impedance mapping technique that can be used to image the inner impedance distribution of the subject under test. Ever since the feasibility of EIT was first reported in the 1980s by Barber and Brown [1], this technique has been intensively researched towards a non-invasive imaging modality for clinical applications [2]-[5].

Patients with respiratory failure often require mechanical ventilation; however, this life-saving therapy can impose other health risks to them. Since 1995, because of better awareness of the risks there has been significant research on lung injury associated with mechanical ventilation, and lung protective ventilation (LPV) strategies have been proposed [6]. These call for patient specific ventilation parameter adjustments (e.g. tidal volume and respiratory rate) that require new tools to better guide the ventilation parameters settings. During respiration, large volumes of conductivity redistribution occur physiologically due to air flow. The use of EIT surrounding the thorax can offer continuous imaging of pulmonary impedance that indicates the distribution of lung behavior during, for example, mechanical ventilation. Thorax EIT is probably the most prominent EIT biomedical application.

The need for LPV is greater for pre-term neonates than for adults. Each year fifteen million babies are born prematurely and many suffer from respiratory failure. Although respiratory support can improve their survival, it could also cause injury to the vulnerable lung. In comparison to conventional imaging techniques such as X-ray and MRI (magnetic resonance imaging), EIT lends itself particularly well for neonatal lung function at the bedside. Clinical EIT has been investigated for lung aeration and ventilation monitoring on neonatal and pediatric patients [7]. Despite the promising results reported, the need for wider and in-depth clinical studies and even daily clinical acceptance of neonatal EIT are still hampered by the quality of images. These are affected by limitations in the hardware and the presence of stray capacitances caused by the passive cable-based patient-electrode interfaces and limited system functionalities [8].

For better EIT performance and more clinically friendly patient-electrode interfaces, active electrodes are employed [9]-[13]. These systems follow the conventional active electrode architecture proposed in the nineties [14]. Before multiplexing the signals to an instrumentation amplifier (IA), active unity
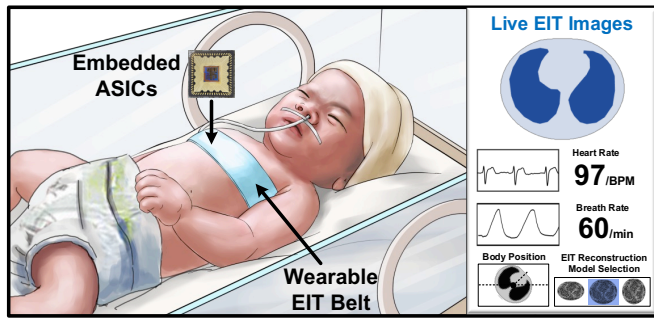
Fig. 1. Concept of the proposed wearable EIT belt with active electrodes for neonatal thorax vital sign monitoring including EIT, ECG, breath rate, position and boundary (torso) shape.

gain buffers are inserted for improved noise immunity but offer little common-mode rejection ratio (CMRR) improvement. Active amplifiers with gain on the electrodes can reduce the noise figure of the analog front-end voltage acquisition [15]. This limits the flexibility of electrode selection for voltage acquisition [16], to recording from only two adjacent electrodes. In this paper a novel active electrode architecture is proposed that overcomes this limitation providing very flexible EIT current drive and voltage sensing patterns with simple digital control and low complexity wiring demand, as well as active gain and higher CMRR. The new high specification active wearable belt is not only capable of wideband EIT operation with high frame rate, but also provides breathing rate, heart rate (ECG), and boundary shape information. This multi-sensing capability is crucial for continuous regional analysis for neonate lung at the bedside as illustrated in Fig. 1.

The rest of the paper is organized as follows. Section II examines the conventional passive and active EIT architectures detailing their limitations, and describes the proposed new active electrode architecture. Section III presents the application specific integrated circuit (ASIC) design. Measured results are presented in Section IV. Section V concludes the paper.

II. EIT SYSTEM ARCHITECTURES

A. Conventional EIT System Architectures

Fig. 2 shows the conventional passive and active electrode systems. In the passive system the electrodes are connected to the analog front-end electronics through switches and shielded cables. The active electrode system places the electronics in close proximity to the skin contact electrode, thus parasitic capacitances are minimized compared to the passive system. As a result, the output impedance and phase delay of the current driver are not compromised. The voltage buffer inserted between the skin-contact electrode and the IA in the hub, Fig. 2(b), offers a high and stable input impedance and transmits recorded signals on a low impedance line which ensures immunity to interference and crosstalk [14], [17]. It is reported in [10], [11], that compared to the passive system [18], [19], the active electrode system offers higher signal-to-noise ratio and less sensitivity to contact impedance variations, allowing EIT in a compact and wearable form. However, present active electrode architectures offer little improvement of CMRR over
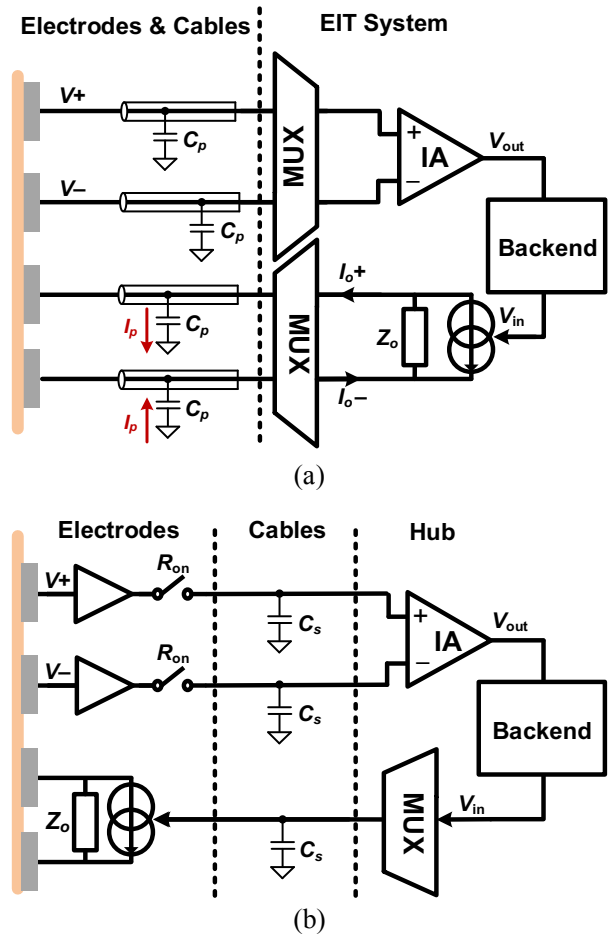

Fig. 2. Conventional EIT system architectures. (a) Using passive electrodes with shielded cable connections. (b) Using active electrodes with differential output current driver and voltage buffers with standard track connections to the hub; $C_s \ll C_p$. In the passive system the large capacitance C_p due the shielded cables shunt diverts current I_p from the load.

the passive system

CMRR is a key specification in any EIT system. Common mode signals experienced by the sense amplifiers (IAs) are inherently caused by the current driver. To obtain a high measurement accuracy (0.1% error) a CMRR of >100 dB for the IA is suggested [20]. Systems employing fully differential drives [21] or complex common mode feedback techniques [22] may reduce common mode signals for enhanced measurement accuracy. A simplified eight electrode EIT phantom model is shown in Fig. 3. The ac current is injected in rotation and on each step differential voltages are sequentially measured. Because the injected current mostly concentrates around the drive electrodes, the potential developed across the adjacent measuring electrodes reduces as they become further away from the current driver. Even with an ideal fully differential current driver, there is still common mode signal between any pair of electrodes. Furthermore, the IA not only measures the differential voltage between electrodes, but also its variations when impedance re-distribution occurs within the subject under test, e.g., variation on V_{6-7} if the value of R_L changes. Any change corresponds to the targeted physiological condition of the subject under test such as lung respiration. High
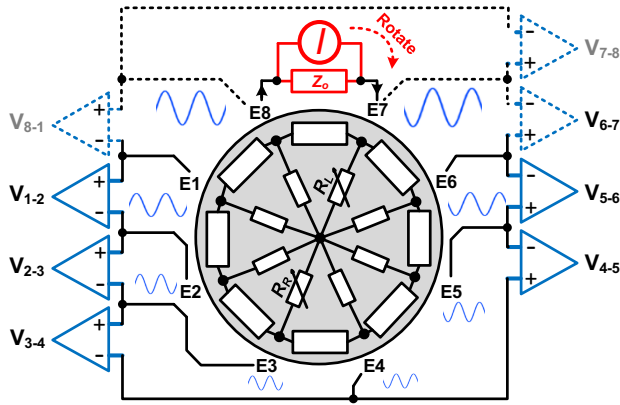
Fig. 3. Simplified EIT model with current drive and voltage recording for an eight electrode system.

performance voltage acquisition front-ends for bioimpedance measurements have been reported [23], [24] but mainly for one-channel recording. Read-out chains for EIT that use current feedback IA for wideband, high CMRR have been also reported [25], [26]. However, (see Fig. 2(a) for example) despite these design efforts, with such complex switching networks and imbalanced cables in front of the IA, a high CMRR is difficult to achieve [27].

B. Proposed Active Electrode Architecture

The new active electrode architecture is shown in Fig. 4. The active electrodes are identical and each uses a fully integrated ASIC. It has five analog switches which are controlled by digital logic. For voltage recording, instead of multiplexing the signals through active buffers, it has an IA in direct contact with the two adjacent electrodes. This approach is an improvement over the active buffer readout architecture in Fig. 2(b) [10], [11], providing superior CMRR. In Fig. 4 the voltage across electrodes 8 and 11 has been chosen as an example of voltage acquisition. Three IAs are switched on to record voltages V_{8-9}, V_{9-10} and V_{10-11} directly from the electrodes, and through MUX4, these voltages are summed by an inverting amplifier (at the bottom of Fig. 4) that provides $V_{sum} = V_8 - V_9 + V_9 - V_{10} + V_{10} - V_{11} = V_{8-11}$. Other IAs which are not required for measurement are switched off and their MUX4 switches connected to ground. Although each IA can only measure its dedicated electrode pair, with a summation readout topology, the system is able to access differential voltages across any pair of selected electrodes with only one readout track. For good matching in the summing circuit resistors with 0.1% tolerance are used.

In this design, any pair of electrodes can be chosen for current injection using a source CD+ on one electrode and a sink CD− on a different electrode (CD− also provides the high common mode signal reduction [28]). During current injection CD+ is excited by an input (differential) signal V_{in} via MUX2. In Fig. 4, electrode 5 (E5) has been chosen to source the current and electrode 2 (E2) to sink it by switching on MUX3. Both source ($I+$) and sink ($I−$) currents are generated by CD+ and CD− in E5. $I−$ is guided by appropriate MUX1, MUX3 and
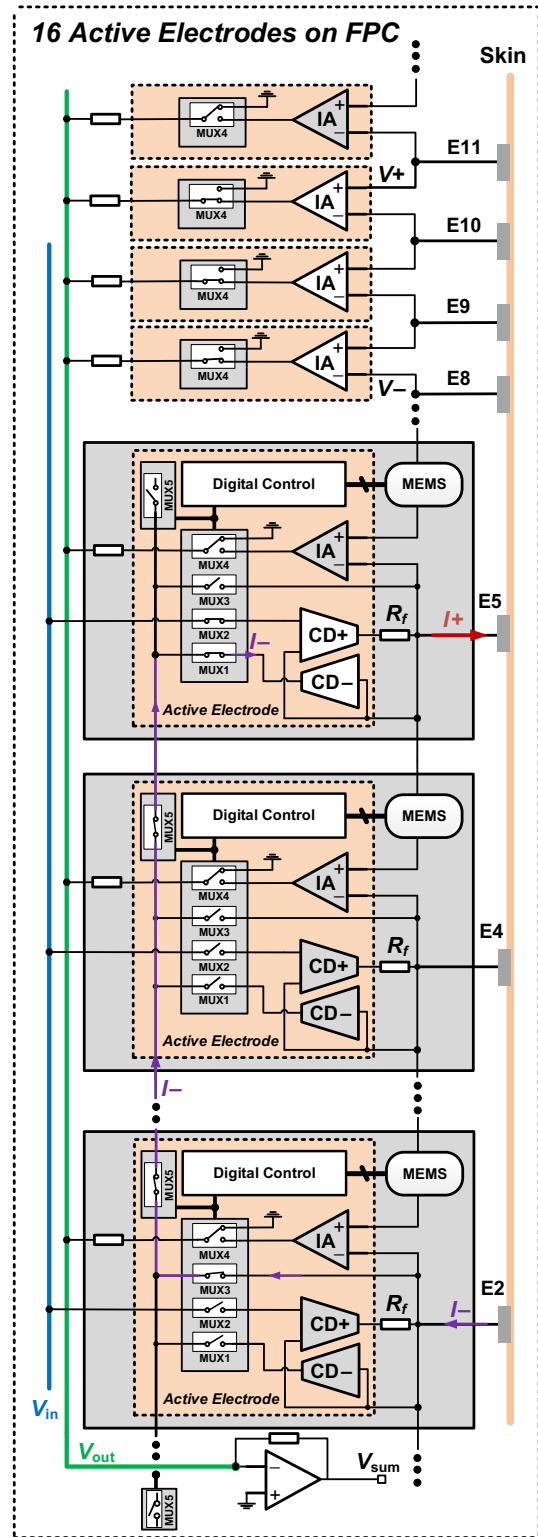

Fig. 4. Proposed active electrode EIT belt architecture with current driver, IA and MEMS shape sensors.

MUX5 switches to E2 to complete the current path (colored in purple). In a given cycle, only one pair of CD+ and CD− are switched on; the other drivers are switched off.

Each ASIC interfaces to a MEMS sensor, designed for tracking the patient's thorax shape and lying position to aid EIT model selection [29]. The ASIC can also measure
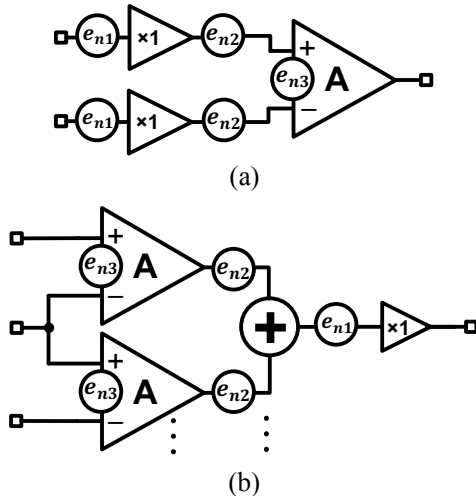
Fig. 5. Noise analysis of the two alternative active EIT system topologies. (a) Buffer topology; (b) IA summing topology.

electrocardiogram waveforms (ECG) providing additional clinical information (see Section III.C).

An important consideration in this type of voltage acquisition is the possibility of added noise in the novel summing topology compared with the buffer topology. Fig. 5 shows the models used for noise analysis of the two voltage acquisition topologies. The gain in both topologies is set to be equal. For the buffer topology [Fig. 5(a)] the input-referred noise is

$$V_{n_{buff}} = \frac{\sqrt{2 \cdot A^2 (e_{n1}^2 + e_{n2}^2) + A^2 \cdot e_{n3}^2}}{A} = \sqrt{2 \cdot (e_{n1}^2 + e_{n2}^2) + e_{n3}^2} \quad (1)$$

where e_{n1} and e_{n3} are the input-referred noise of active buffer and the IA in the hub respectively, and e_{n2} is the noise coupled to the tracks while transmitting signals back to the hub. Assuming $e_{n1} = e_{n3}$ then

$$V_{n_{buff}} = \sqrt{3 \cdot e_{n1}^2 + 2 \cdot e_{n2}^2}. \quad (2)$$

For the IA summing topology, the input-referred noise is

$$V_{n_{IA}} = \frac{\sqrt{m \cdot A^2 \cdot e_{n3}^2 + m \cdot e_{n2}^2 + e_{n1}^2}}{A}$$
$$= \sqrt{m \cdot e_{n3}^2 + \frac{m \cdot e_{n2}^2}{A^2} + \frac{e_{n1}^2}{A^2}} \approx \sqrt{m \cdot e_{n3}^2} \quad (3)$$

where e_{n1} and e_{n3} are the input-referred noise of the summing amplifier and active IAs respectively, e_{n2} is the noise coupled to the tracks plus thermal noise of the input resistors used in the summing amplifier, and m is the number of IAs used for summation.

From the above equations, assuming $e_{n1} = e_{n3}$ and e_{n2} is neglected, for $m < 3$ the IA summing topology has less noise than the buffer topology. In EIT measurement, the most frequently used drive pattern uses adjacent electrodes (as illustrated in Fig. 3), with no electrode offset ($m = 1$). Other current injection patterns have been investigated [30] and results suggest those which involve large electrode should be avoided. However, a better image could be obtained with a suitable electrode offset selected for special targeted applications. When a high number of IAs are used in
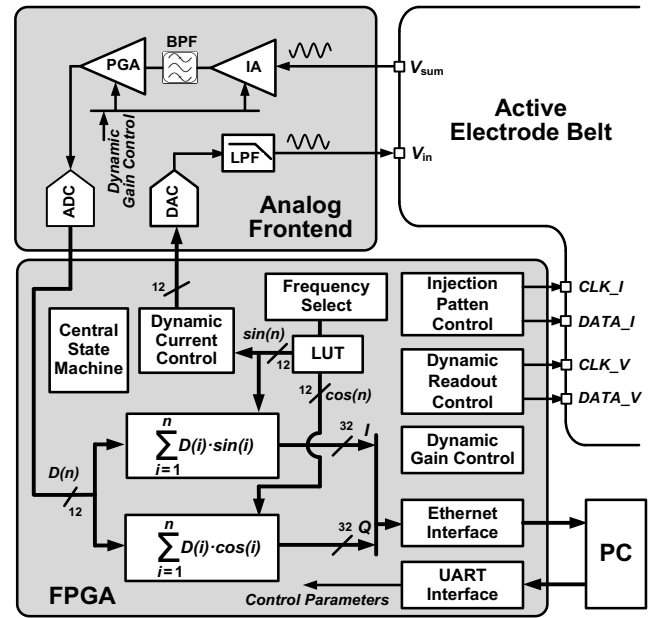

Fig. 6. System architecture of the central hub for EIT measurement.

summation, a design trade-off must be made between CMRR and noise.

C. Central Hub of EIT System

Operation control and signal conditioning of the proposed EIT system is carried out in a central hub. Fig. 6 shows the system architecture of the central hub. In operation, the digital control module reads out from a look-up table (LUT) a 12-bit data stream of a pre-stored single tone sinusoidal waveform. The data stream is converted into an analog sinusoidal signal, V_{in}, by a 12-bit digital-to-analog converter (DAC) at 32 MSps. This sinusoidal signal excites the current driver in one of the 16 active electrodes, as shown in Fig. 4 and Fig. 6. The address of the LUT readout is programmable so that the frequency of V_{in} can be selected as 125 kHz, 250 kHz, 500 kHz and 1 MHz. The output voltage from the active electrode belt, V_{sum}, is further amplified first by an IA and then a programmable gain amplifier (PGA). The amplified voltage is digitized by a 12-bit analog-to-digital converter (ADC) at 32 MSps into a data stream, $D(n)$, where the real and imaginary vectors, I and Q, of each electrode voltage readout are derived from $D(n)$ with digital quadrature demodulation. I and Q are sent to a PC in real time via a 100 Mbps Ethernet interface for image reconstruction.

The digital control module is implemented on a Xilinx Artix-7 FPGA. The operation of the digital control, including LUT readout, ADC digitization, quadrature demodulation and active electrode control, is synchronized by a central state machine operating at 64 MHz. The analogue frontend is built with commercially off-the-shelf (COTS) components.

1) Active Electrode Control:

The central hub selects the active electrodes for current injection and voltage recording via two parallel control bus as shown in Fig. 6, generated by the injection pattern control module and the readout pattern control module, respectively. Both modules generate a clock to shift a 16-bit stream through

This article has been accepted for publication in a future issue of this journal, but has not been fully edited. Content may change prior to final publication. Citation information: DOI 10.1109/TBCAS.2019.2925713, IEEE Transactions on Biomedical Circuits and Systems
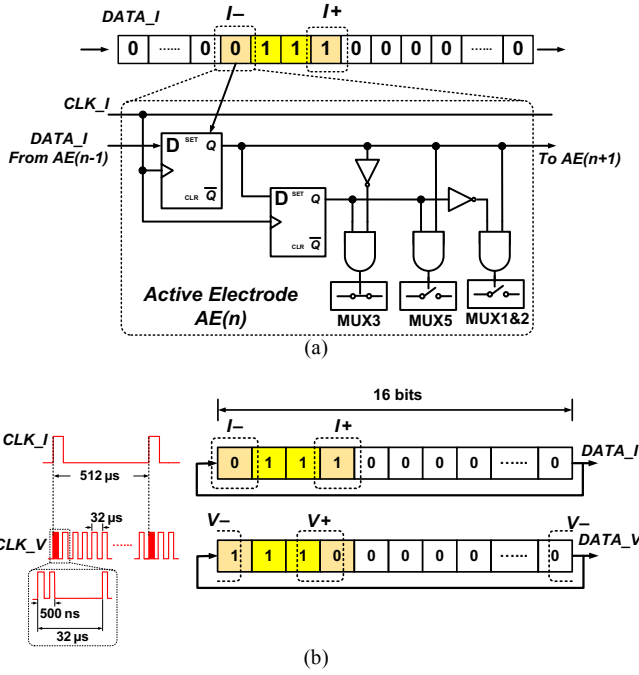
5

(a)

(b)

Fig. 7. Active electrode control. (a) Injection control logic in the active electrode (AE); (b) Illustration of injection pattern control and readout pattern control in the central hub.

the daisy-chain connected registers in the active electrode digital control, where the section of consecutive number of bit '1' decides the injection and recording electrodes. Fig. 7(a) shows the active electrode digital control for the current injection which compares the register current state with the new state to set current drive to source, sink or at idle. The active electrode for voltage sensing is controlled by the current bit of *DATA_V* on each active electrode and at '1' the active electrode IA and MUX4 are turned on.

The clocks for injection pattern control and readout pattern control, *CLK_I* and *CLK_V*, are synchronized. The period of *CLK_I* is 16 times the period of and *CLK_V*, as shown in Fig. 7(b). Two 16-bit ring counters in the two pattern control modules shift at the two clocks respectively, where the lowest bits of both counters are sent to the daisy chains on the active electrode belt. Therefore, for each pair of current injection electrodes, voltage sensing can complete a full cycle around the 16 electrodes. The period of *CLK_I* is set to 512 μs, giving a frame rate of 122 fps. The initial value of the two ring counters can be set from the UART interface to achieve flexible injection and recording patterns.

2) Dynamic Voltage and Current Controls:
The gains of the IA and PGA in the HUB can be changed dynamically within a voltage scan cycle according to the relative position of the current injecting and voltage recording electrodes. The gains can be relatively low when the recording electrodes are close to the injection electrodes, and high when the recording electrodes are further away (see Fig. 3). This allows efficient use of the ADC input dynamic range for voltage readout at each electrode pair. For this purpose, there are two consecutive *CLK_V* pulses within 500 ns at the beginning of every voltage scan cycle. Therefore, a voltage scan cycle
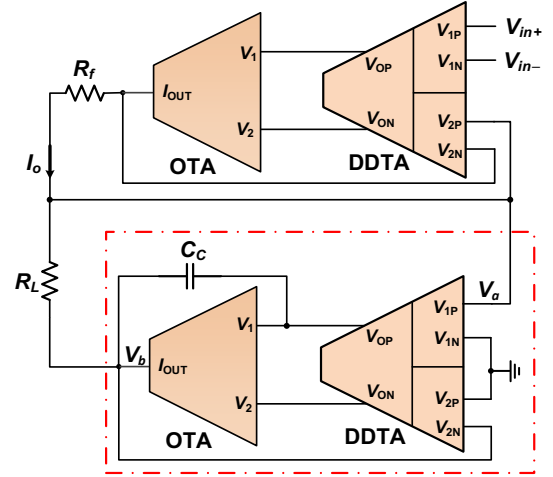

Fig. 8. The fully differential current driver implemented in the ASIC driving a load R_L.

always starts with *V–* aligning with *I–*, as shown in Fig. 7(b), regardless the position of the current injection electrodes. With this arrangement, the relative position between the current injecting and voltage recording electrodes, hence the dynamic gain settings, always follows the same pattern in a voltage scan cycle, which repeats 16 times in an image frame. This simplifies the hardware implementation of dynamic gain control, where up to 16 gain settings for the IA and PGA can be set to the digital control module via the UART interface.

In order to avoid large voltages on the injection electrodes saturating the corresponding IAs, dynamic current control is applied. In every *CLK_V* cycle, a bitwise AND operation is applied with the values in the two ring counters for *DATA_I* and *DATA_V*. In case of a non-zero result, which indicates one or both of the current injection electrodes are involved in voltage acquisition, the peak-to-peak value of the waveform from the LUT is attenuated to reduce the amplitude of the injection current.

III. Active Electrode ASIC

A. Current Driver

The current driver consists of a source driver CD+ and a sink driver CD– for fully differential drive. The CMOS circuit implementation is adapted from [13].

Fig. 8 shows the drivers. They are based on the same building block namely a differential difference transconductance amplifier (DDTA), and an operational transconductance amplifier (OTA). CD+ (top) is connected in current feedback where its output current is set by $I_o = (V_{\text{in}+} - V_{\text{in}-})/R_f$. CD– (within the red box) is connected in common mode feedback. By sinking a current matching the source current CD+, CD– provides a voltage potential $V_b \approx -V_a$, so that the load R_L is floating with minimal common mode signal. Capacitor C_c is added for loop stability.

B. Voltage Acquisition Circuit

The circuit is formed by two building blocks. A current feedback IA front-end and an output buffer to provide low output impedance to avoid stray capacitance distortion in the
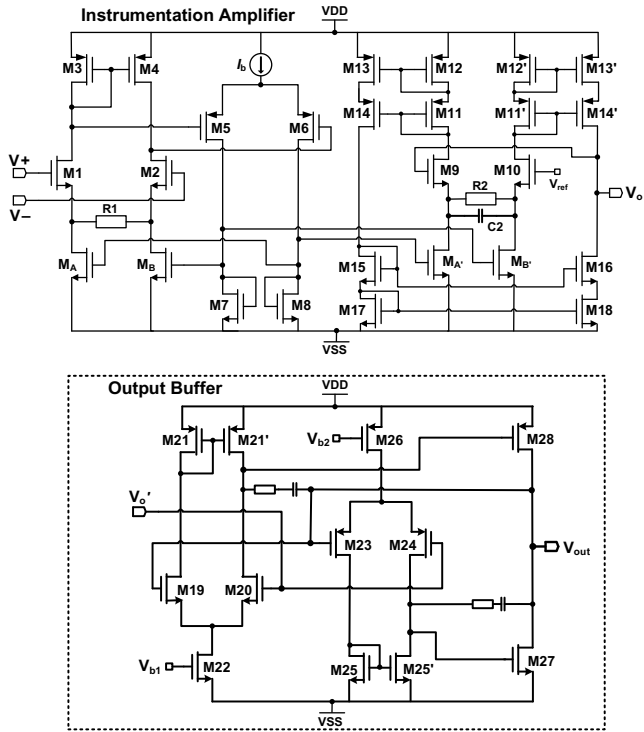
Fig. 9. Current feedback IA CMOS level implementation with output buffer.

Fig. 10. (a) Boundary shape detection for EIT model selection using MEMS. (b) ECG measurement for heart rate monitoring.

connecting tracks. The circuit CMOS level implementation is shown in Fig. 9.

The IA is based on a current feedback topology [26]. It has an input transconductance stage with a source degenerative resistor R_1. The input stage also has a local feedback current loop M5 to M8. This feedback serves to set the current in M1 and M2 to be equal by adjusting the current in MA and MB. The input differential voltage is then reflected across R_1 which causes a current difference in MA and MB corresponding to this voltage difference. At the output stage of the IA, another transconductor mirrors the current difference in MA′ and MB′ which is reflected in resistor R_2. The gate terminal of M10 connects to a reference voltage, $V_{REF} = 0$ V, and by connecting the gate of M9 to the output V_o', forms a feedback loop which adjusts the gate voltage of M9 until the current in both M9 and M10 are equal. This results in an output voltage $V_o' = (V_+ - V_-) \cdot (R_2/R_1)$. Resistor R_2 and capacitor C_2 set the bandwidth of the IA to $f_{-3dB} = 1/(2\pi R_2 C_2)$. The symmetrical structure of this IA topology enables a high CMRR to be achieved by careful symmetrical layout that mitigates the effect of process variations.

The IA is followed by an output stage which is implemented as a common-drain push-pull buffer whose circuit details are given in Fig. 9. M19 to M22 and M23 to M26 form two error amplifiers which operate in feedback to regulate the current in the common-drain transistors M27 to M28 and forces the output voltage to be the same as the input voltage. Due to the push-pull topology the buffer can provide large current outputs to drive capacitive loads with a low output impedance

$$Z_O = \frac{\frac{1}{g_{oM37}} + \frac{1}{g_{oM38}}}{1 + A_{\text{open\_loop}}} \quad (4)$$
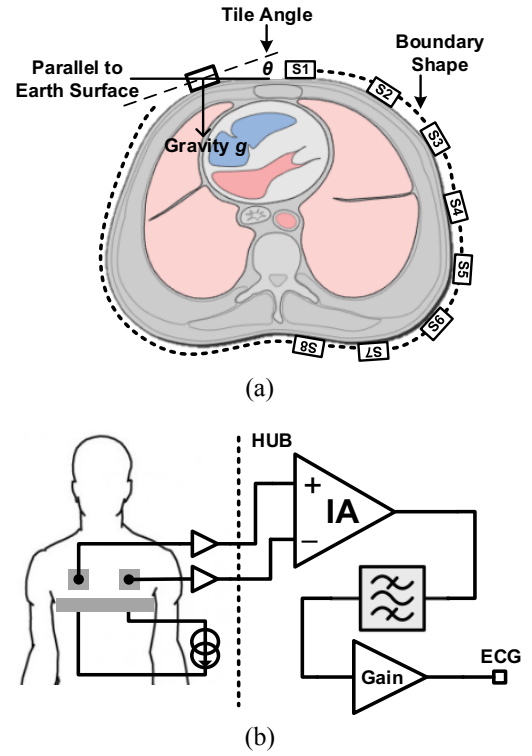
where g_{oM37} and g_{oM38} are drain conductances, and $A_{\text{open\_loop}}$ is the open loop gain of the error amplifier.

C. Heart Rate Recording and Shape Sensing

In EIT, boundary shape information can be used to improve EIT algorithms. Conventionally, a single representative boundary model is obtained from CT scans and used for all patients. This one-size-fits-all practice can lead to image artifacts [29]. An EIT belt that can monitor boundary (torso) shapes in real-time when the patient is laying in different positions could significantly improve the EIT image quality. Through the multiplexers in the ASICs, the hub could selectively communicate with any MEMS accelerometer (ADXL313) for patient boundary shape detection as shown in Fig. 10(a). The boundary shape is detected by calculating the accelerometer tilt angle with respect to earth surface, and because the relative position of each accelerometer is known, a patient specific shape can be identified.

In each ASIC, there is an extra voltage buffer and by selecting two buffers, an ECG signal can be measured using an IA in the hub to extract heart rate as shown in Fig. 10(b). Because the current driver biases the body to a known potential, a third lead is no longer required during the ECG recording

IV. MEASURED RESULTS

A. Active Electrode ASIC

The ASIC was designed in 0.35-μm CMOS HV process technology and operates from ±9 V (analog) and 3.3 V (digital) power supplies. The power consumption of the ASIC is about 250 mW at maximum drive current. The ASIC micrograph is

TABLE I. ASIC MEASURED PERFORMANCE

	Transconductance (mA/V)	Bandwidth (Hz)	Phase (at 1 MHz)	Z_{out} (at 1 MHz)	I_{out} Maximum	THD (at 1 MHz)	Voltage Compliance
Current Driver	1.99	1 M	12°	507 kΩ	6 mA$_{p-p}$	43 dB	10 V$_{p-p}$

	Gain (V/V)	Bandwidth (Hz)	Phase (at 1 MHz)	CMRR (at 1 MHz)	Input Range	THD (at 1 MHz)	Input-Referred Noise (Bandwidth)
Instrumentation Amplifier	10.5	1 M	23°	74 dB	300 mV$_{p-p}$	42.5 dB	25.8 µV$_{rms}$ (0.05-1 MHz)

Fig. 11. Active electrode ASIC micrograph.

Fig. 12. System impedance measurement accuracy. The solid black lines are the measured values and the blue dotted lines are the ideal values.
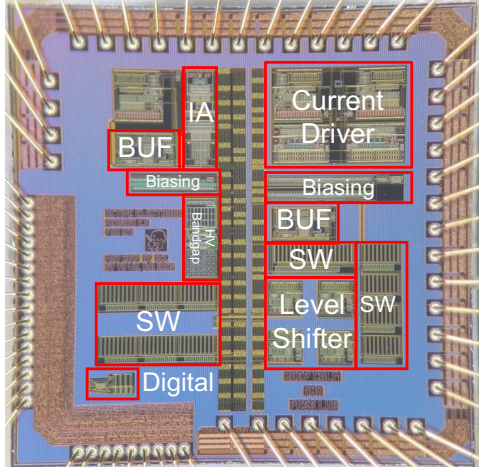
shown in Fig. 11 with the various blocks labeled. The total area is 3.1 mm × 3.1 mm. Table I summarizes the measured performance of the ASIC.

B. System Performance Test

EIT is fundamentally a bio-impedance measurement device. To verify the system performance, impedance measurement tests were carried out for all possible channels to investigate measurement accuracy, channel variations and system SNR. For a 16-electrode system, there are 208 channels, and it can measure impedances at 125 kHz, 250 kHz, 500 kHz and 1 MHz. In this test, a parallel R-C load where $R = 99\ \Omega$ and $C = 2.88\ n$F was used. The measured results are plotted in Fig. 12 in solid black lines for both impedance amplitude and phase along with the ideal value given in dotted blue lines. Across the frequency band, on average, the system has an impedance measurement accuracy of 98.9%, and a phase measurement accuracy of 98.2%. The red error bars in Fig. 12 show the maximum spread across all 208 channels at a given frequency. The measured variance on impedance amplitude is ±0.49 Ω and the phase variance is ±0.77°. With the same R-C load, the system SNR is measured using

$$\text{SNR} = 10 \cdot \log \frac{\sum_{n=1}^{N}[x_n]^2}{\sum_{n=1}^{N}[x_n - x_{\text{avg}}]^2}. \tag{5}$$

where $N = 10$ and is the total number of data sets used, x_n is the measurement data from the nth channel and x_{avg} is the average data value of the N datasets. The SNR on average across all channels is 54.3 dB at 125 kHz and drops to 48.4 dB at 1 MHz.

To illustrate the merit of the proposed active electrode architecture, a comparison is made between three eight-
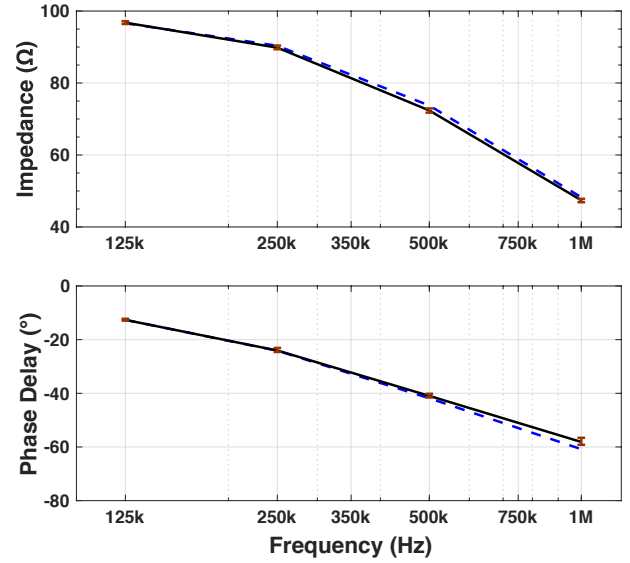

(a) Ideal Image   **(b) Passive**
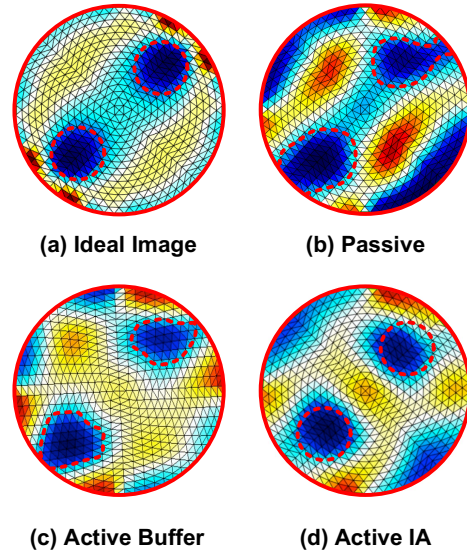
(c) Active Buffer   **(d) Active IA**

Fig. 13. Comparison between three different 8-electrode EIT systems. (a) Ideal EIT image; (b) Passive EIT system; (c) Active buffer EIT system; (d) Proposed active IA EIT system.

electrode EIT systems using different architectures, namely the passive, active buffer, and the proposed active IA. All three systems were tested on the same resistive phantom [31] which has two diagonal inner resistive elements (see Fig. 3 for
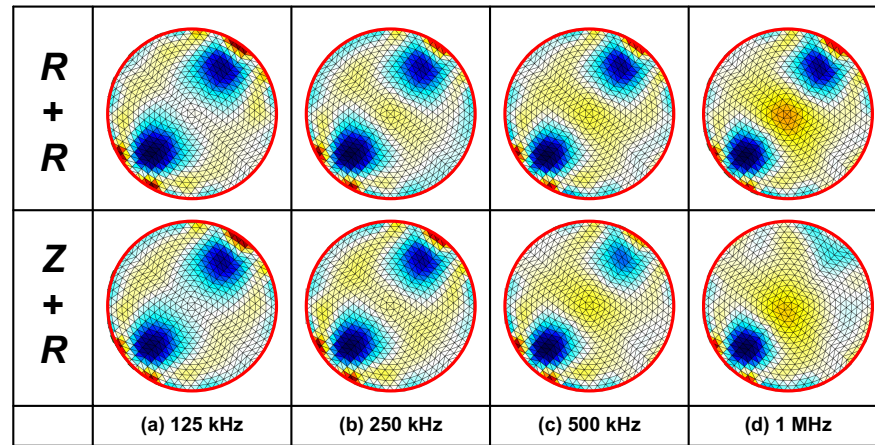
Fig. 14. The 16-electrode system phantom image results at 125 kHz, 250 kHz, 500 kHz and 1 MHz. $R + R$ is two identical resistive elements R_L and R_R at diagonal positions. $Z + R$ is one resistive element R_L and an R-C impedance load Z_R at diagonal positions.
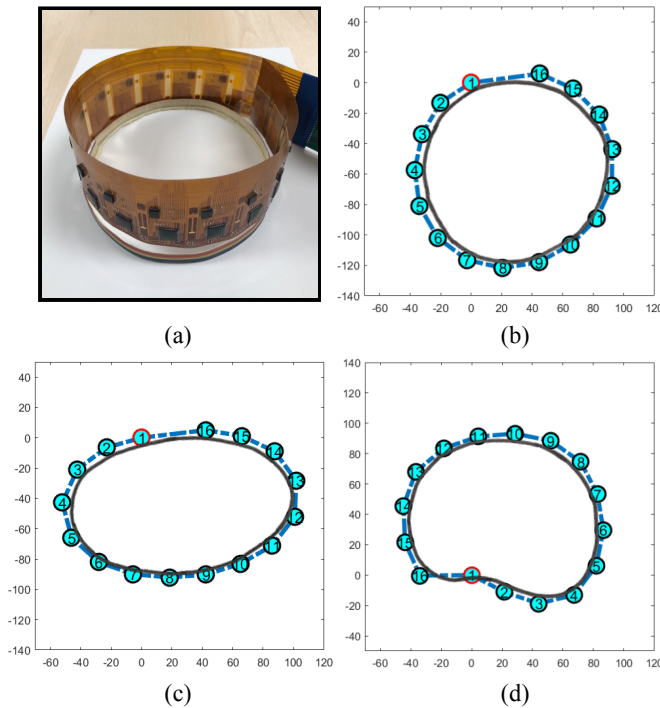

Fig. 15. Shape measurements. (a) The belt is wrapped on the contour; (b) circle shape; (c) oval shape; (d) distorted shape. The shapes have been reconstructed compared to the reference contours (black lines). The blue lines are the reconstructed shapes.
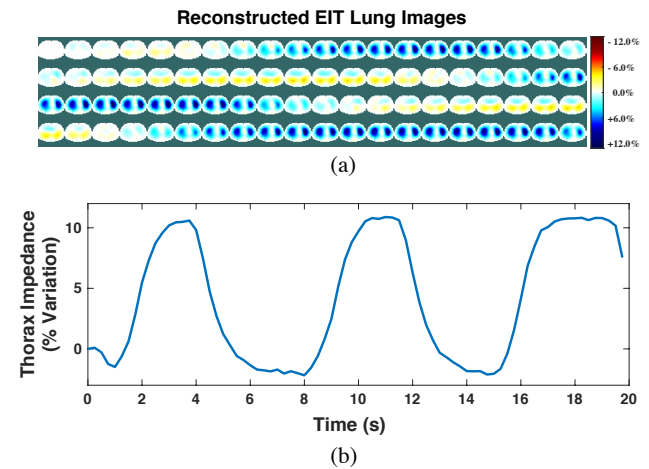

Fig. 16. *In-vivo* measurements. (a) Eighty reconstructed EIT lung images showing inhalation and exhalation; (b) Breathing cycle corresponding to the EIT images in (a).
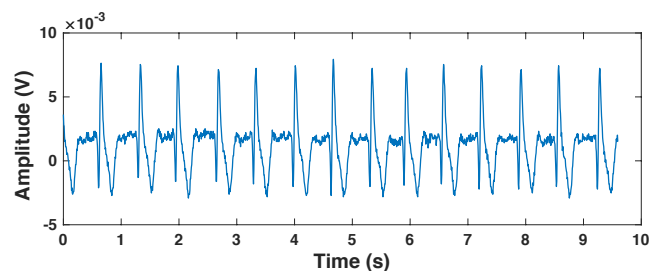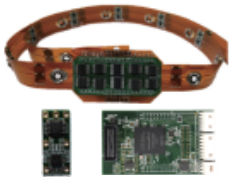

Fig. 17. The ECG measurements for heart rate monitoring.

reference) R_L and R_R which represent the 'objects' inside the phantom. Fig. 13(a) is the EIT image using simulation data as reference for comparison. Fig. 13(b) is the image obtained from a passive system, Fig. 13(c) is the image obtained from an active buffer system, and Fig. 13(d) is from the proposed IA based architecture implementation. The active IA is a superior match to the ideal.

For the 16-electrode system imaging test, the phantom is measured from 125 kHz to 1 MHz and the results are shown in Fig. 14. In the $R + R$ row, two 45 Ω resistive elements are used for both R_L and R_R to represent the diagonal phantom 'objects'. When the phantom is purely resistive, all the images should look the same across the frequency spectrum.

However, tissues are modeled as a combination of R-C elements, and for different types of tissues or due to certain clinical conditions, they vary differently with respect to frequency. In Fig. 14, for the $Z + R$ row, the phantom is modified with R_R and Z_R at the two diagonal positions. $R_L = 45$ Ω but Z_R is a R-C parallel impedance where $R = 68$ Ω, $C = 21$ nF. The effect of Z_R is demonstrated when multi-frequency images are applied. The phantom 'object' corresponding to Z_R fades away as the frequency increases due to its reactive

TABLE II. COMPARISON WITH OTHER WEARABLE EIT SYSTEMS

Wearable EIT System for Lung Function Monitoring	2015 – Swisstom [9]	2018 – KHU [11]	2018 – CRADL v1.0 [13]	This Work – CRADL v2.0
Number of electrodes	32	16	32	16
Active electrodes	Yes	Yes	Yes	Yes
Active electrode configuration	Unity gain buffer	Unity gain buffer	Unity gain buffer and current driver	Active gain, high CMRR IA and current driver
EIT scan pattern	N/A	N/A	Programmable	Programmable
Frequency	150 kHz	11.25 kHz	50 kHz – 500 kHz	45 kHz – 1 MHz
Current amplitude	50% of I_{max} [1]	2.8 mA_{p-p}	≤ 6 mA_{p-p}	≤ 6 mA_{p-p}
Frame rate	50 fps	25 fps	107 fps	122 fps
Multi-frequency operation	No	No	No	Yes
Heart rate	No	Yes	Yes	Yes
Torso shape tracking	No	No	Yes	Yes

[1] Maximum patient auxiliary current conforming to IEC 60601-1.

component. This phenomenon is significant at 1 MHz. It cannot be detected at 125 kHz because the impedance value of Z_R is also ~45 Ω at that frequency. In clinical applications, different tissues or conditions (e.g. pulmonary edema) can be identified by observing the EIT images over a wide bandwidth. These results not only demonstrate that the proposed system can image accurately up to 1 MHz when compared to the ideal image, but also show the importance of a wide EIT bandwidth for impedance differentiation.

C. Boundary Shape Detection

The shape measurement test is shown in Fig. 15(a); a variety of contour shapes are created. A test belt containing the ASICs and MEMS is wrapped around these contours for shape measurement, the contour shapes are recorded and compared with the shapes reconstructed from the MEMS. As shown in Fig. 15 three shapes, circle, oval and torso were tested. The black line is the reference contour and the dotted line is the reconstructed shape with each MEMS sensor labelled. By identifying the sensors, the belt orientation could also be observed. In Fig. 15(d), the belt is rotated by 100 degrees compared to Fig. 15(c).

D. System in-Vivo Validation

The *in-vivo* test was carried out on an adult volunteer using a larger size belt. The belt was covered with the textile dressing, made of two interdigitated stripes, one being silver coated fabric and the other is insulative. The silver coated stripes are the electrodes that make the contact with the skin. A detailed description of the belt construction is given in previous work [13]. The volunteer was asked to breathe normally while EIT measurements were taken. Eighty frames of lung respiration EIT images are reconstructed in Fig. 16(a). The EIT images show lung respiration changes in a cross-section view, the colour scale on the right-hand side indicates the impedance variation as a percentage compared to the reference baseline

(the first frame). The color maps from red to blue indicate the regions that are more conductive (red) or resistive (blue). During inhalation, the lung is inflated and this results in impedance increments in the chest region. The regions have impedance increments and the level of such increments is illustrated by the area and intensity of blue scaled colours on the EIT image and vice-versa. The thorax impedance variation is with respect to the reference frame, and it is plotted in Fig. 16(b). It corresponds to the EIT images in Fig. 16(a) and can be used to identify the breathing cycle, e.g. a longer breath was held after the third inhalation. The ECG was also measured on the volunteer and the result is shown in Fig. 17. The ECG signal is recorded for heart rate monitoring. ECG is an important vital sign needing to be monitored for patients in intensive care.

E. Comparison With Other Work

Table II compares state-of-the-art wearable EIT systems for lung function monitoring. The proposed system is highly integrated with a novel active electrode architecture which improves signal accuracy and EIT image quality. This system has the widest bandwidth of 1 MHz and the highest image frame rate of 122 fps. In addition, it offers very flexible programmable electrode patterns for current injection and voltage measurement and multi-frequency operation. It also incorporates other important clinical features in an integrated wearable belt.

V. CONCLUSION

A programmable, wearable EIT belt for neonatal thorax vital multiple sign monitoring has been developed. It can provide high quality information concerning lung respiration, breathing cycle, heart rate, and potentially boundary shape. Unlike other active electrode EIT systems, it features a novel IA based summation architecture with a high-performance ASIC providing superior common-mode rejection ratio while

reducing the complexity of wiring and digital control. The system has a fast image frame rate of 122 fps, a wide bandwidth of 1 MHz, and multi-frequency operation. It can measure impedance with 98% accuracy within less than 0.5 Ω and 1° variations across all channels. The EIT image results demonstrated the merits of the new system architecture and the benefit of wideband EIT.

REFERENCES

[1] B. H. Brown, D. C. Barber, and A. D. Seagar, "Applied potential tomography: Possible clinical applications," *Clin. Phys. Physiol. Meas.*, vol. 6, no. 2, pp. 109–121, 1985.

[2] M. Konijnenburg et al., "A battery-powered efficient multi-sensor acquisition system with simultaneous ECG, BIO-Z, GSR, and PPG," in *Proc. ISSCC*, San Francisco, CA, 2006, pp. 480–481.

[3] M. S. Campisi, C. Barbre, A. Chola, G. Cunningham, V. Woods, and J. Viventi, "Breast cancer detection using high-density flexible electrode arrays and electrical impedance tomography," in *Proc. EMBS*, Chicago, IL, 2014, pp. 1131–1134.

[4] H. Li, B. Liu, Y. Li, G. Wang, and Y. Lian, "A high accuracy and high sensitivity system architecture for electrical impedance tomography system," in *Proc. APCCAS*, Chengdu, China, 2018, pp. 155–158.

[5] Y. Wu, D. Jiang, X. Liu, R. Bayford, and A. Demosthenous, "A human-machine interface using electrical impedance tomography for hand prosthesis control," *IEEE Trans. Biomed. Circuits Syst.*, vol. 12, no. 6, pp. 1322–1333, 2018.

[6] A. Adler et al., "Whither lung EIT: Where are we, where do we want to go and what do we need to get there?," *Physiol. Meas.*, vol. 33, no. 5, pp. 679–694, 2012.

[7] I. Frerichs et al., "Chest electrical impedance tomography examination, data analysis, terminology, clinical use and recommendations: Consensus statement of the TRanslational EIT developmeNt stuDy group," *Thorax*, vol. 72, no. 1. pp. 83–93, 2017.

[8] A. McEwan, G. Cusick, and D. S. Holder, "A review of errors in multi-frequency EIT instrumentation," *Physiol. Meas.*, vol. 28, no. 7, pp. S197–215, 2017.

[9] Swisstom, "Swisstom BB2 Product Information," Rev.004, 2013. [Online]. Available: http://www.swisstom.com/en/products/swisstom-bb2_en. [Accessed: 15-Apr-2019].

[10] P. O. Gaggero, A. Adler, J. Brunner, and P. Seitz, "Electrical impedance tomography system based on active electrodes," *Physiol. Meas.*, vol. 33, no. 5, pp. 831–847, 2012.

[11] M. H. Lee et al., "Portable multi-parameter electrical impedance tomography for sleep apnea and hypoventilation monitoring: Feasibility study," *Physiol. Meas.*, vol. 39, no. 12, p. 124004, 2018.

[12] M. Rapin et al., "Wearable sensors for frequency-multiplexed EIT and multilead ECG data acquisition," *IEEE Trans. Biomed. Eng.*, vol. 66, no. 3, pp. 810–820, 2019.

[13] Y. Wu, D. Jiang, A. Bardill, S. De Gelidi, R. Bayford, and A. Demosthenous, "A high frame rate wearable EIT system using active electrode ASICs for lung respiration and heart rate monitoring," *IEEE Trans. Circuits Syst. I: Regular Papers*, vol. 65, no. 11, pp. 3810–3820, 2018.

[14] B. Rigaud, Y. Shi, N. Chauveau, and J. P. Morucci, "Experimental acquisition system for impedance tomography with active electrode approach," *Med. Biol. Eng. Comput.*, vol. 31, no. 6, pp. 593–599, 1993.

[15] M. Kim et al., "A 1.4-m Ω-sensitivity 94-dB dynamic-range electrical impedance tomography SoC and 48-channel hub-SoC for 3-D lung ventilation monitoring system," *IEEE J. Solid-State Circuits*, vol. 52, no. 11, pp. 2829–2842, 2017.

[16] A. Adler, P. O. Gaggero, and Y. Maimaitijiang, "Adjacent stimulation and measurement patterns considered harmful," *Physiol. Meas.*, vol. 32, no. 7, pp. 731–744, 2011.

[17] J. Xu, S. Mitra, C. Van Hoof, R. F. Yazicioglu, and K. A. A. Makinwa, "Active electrodes for wearable EEG acquisition: Review and electronics design methodology," *IEEE Rev. Biomed. Eng.*, vol. 10. pp. 187–198, 2017.

[18] H. Wi, T. I. Oh, A. L. McEwan, E. J. Woo, and H. Sohal, "Multi-frequency electrical impedance tomography system with automatic self-calibration for long-term monitoring," *IEEE Trans. Biomed. Circuits Syst.*, vol. 8, no. 1, pp. 119–128, 2013.

[19] Y. Yang and J. Jia, "A multi-frequency electrical impedance tomography system for real-time 2D and 3D imaging," *Rev. Sci. Instrum.*, vol. 88, no. 8, p. 085110, 2017.

[20] J. Rosell and P. Riu, "Common-mode feedback in electrical impedance tomography," *Clin. Phys. Physiol. Meas.*, vol. 13, pp. 11–14, 1992.

[21] J. Liu, X. Qiao, M. Wang, W. Zhang, G. Li, and L. Lin, "The differential Howland current source with high signal to noise ratio for bioimpedance measurement system," *Rev. Sci. Instrum.*, vol. 85, no. 5, p. 055111, 2014.

[22] P. J. Langlois, Y. Wu, R. H. Bayford, and A. Demosthenous, "On the application of frequency selective common mode feedback for multifrequency EIT," *Physiol. Meas.*, vol. 36, no. 6, pp. 1337–1350, 2015.

[23] N. Van Helleputte et al., "A 345 µW multi-sensor biomedical SoC with bio-impedance, 3-channel ECG, motion artifact reduction, and integrated DSP," *IEEE J. Solid-State Circuits*, vol. 50, no. 1, pp. 230–244, 2015.

[24] J. Xu et al., "A 36 µW 1.1 mm^2 reconfigurable analog front-end for cardiovascular and respiratory signals recording," IEEE Trans. Biomed. Circuits Syst., vol. 12, no. 4, pp. 774–783, 2018.

[25] M. Takhti, Y. C. Teng, and K. Odame, "A 10 MHz read-out chain for electrical impedance tomography," *IEEE Trans. Biomed. Circuits Syst.*, vol. 12, no. 1, pp. 222–230, 2018.

[26] A. Worapishet, A. Demosthenous, and X. Liu, "A CMOS instrumentation amplifier with 90-dB CMRR at 2-MHz using capacitive neutralization: Analysis, design considerations, and implementation," *IEEE Trans. Circuits Syst. I: Regular Papers*, vol. 58, no. 4, pp. 699–710, 2011.

[27] R. C. Jaeger, "CMRR performance limits of analog multiplexers using normal-mode filters," *IEEE Trans. Instrum. Meas.*, vol. IM–30, no. 2, pp. 129–132, 1981.

[28] Y. Wu, D. Jiang, P. Langlois, R. Bayford, and A. Demosthenous, "A CMOS current driver with built-in common-mode signal reduction capability for EIT," in *Proc. ESSCIRC*, Leuven, Belgium, 2017, pp. 227–230.

[29] S. De Gelidi et al., "Torso shape detection to improve lung monitoring," *Physiol. Meas.*, vol. 39, no. 7, p. 74001, 2018.

[30] S. Russo, S. Nefti-Meziani, N. Carbonaro, and A. Tognetti, "A quantitative evaluation of drive pattern selection for optimizing EIT-based stretchable sensors," *Sensors*, vol. 17, no. 9, p. 1999, 2017.

[31] Swsstom.AG, "ResistorPhantomManual 1ST504-103," Rev 000, 2013. [Online]. Available: http://www.swisstom.com/software/PDF/ResistorPhantomManual_1ST 504-103_Rev_000.pdf. [Accessed: 03-May-2019].